Biomedical Optics EXPRESS

Third harmonic generation imaging for fast, label-free pathology of human brain tumors

N. V. Kuzmin,[1,2,*] P. Wesseling,[3,4,6] P. C. de Witt Hamer,[5,6] D. P. Noske,[5,6] G. D. Galgano,[1] H. D. Mansvelder,[2] J. C. Baayen,[5] and M. L. Groot[1,2]

[1]LaserLab Amsterdam, VU University, De Boelelaan 1081, 1081 HV Amsterdam, The Netherlands
[2]Neuroscience Campus Amsterdam, VU University, De Boelelaan 1085, 1081 HV Amsterdam, The Netherlands
[3]Dept. of Pathology, VU University Medical Center, De Boelelaan 1117, 1081 HV Amsterdam, The Netherlands
[4]Dept. of Pathology, Radboud University Medical Center, Geert Grooteplein Zuid, 6525 GA Nijmegen, The Netherlands
[5]Dept. of Neurosurgery, VU University Medical Center, De Boelelaan 1117, 1081 HV Amsterdam, The Netherlands
[6]Amsterdam Brain Tumor Center, VU University Medical Center, De Boelelaan 1117, 1081 HV Amsterdam, The Netherlands
[*]n.v.kuzmin@vu.nl

Abstract: In brain tumor surgery, recognition of tumor boundaries is key. However, intraoperative assessment of tumor boundaries by the neurosurgeon is difficult. Therefore, there is an urgent need for tools that provide the neurosurgeon with pathological information during the operation. We show that third harmonic generation (THG) microscopy provides label-free, real-time images of histopathological quality; increased cellularity, nuclear pleomorphism, and rarefaction of neuropil in fresh, unstained human brain tissue could be clearly recognized. We further demonstrate THG images taken with a GRIN objective, as a step toward *in situ* THG microendoscopy of tumor boundaries. THG imaging is thus a promising tool for optical biopsies.

©2016 Optical Society of America

OCIS codes: (180.4315) Nonlinear microscopy; (190.4160) Multiharmonic generation; (170.4730) Optical pathology; (170.6935) Tissue characterization; (170.1530) Cell analysis; (170.2150) Endoscopic imaging.

References and links

1. N. G. Burnet, S. J. Jefferies, R. J. Benson, D. P. Hunt, and F. P. Treasure, "Years of life lost (YLL) from cancer is an important measure of population burden--and should be considered when allocating research funds," Br. J. Cancer **92**(2), 241–245 (2005).
2. J. A. Schwartzbaum, J. L. Fisher, K. D. Aldape, and M. Wrensch, "Epidemiology and molecular pathology of glioma," Nat. Clin. Pract. Neurol. **2**(9), 494–516 (2006).
3. J. S. Smith, E. F. Chang, K. R. Lamborn, S. M. Chang, M. D. Prados, S. Cha, T. Tihan, S. Vandenberg, M. W. McDermott, and M. S. Berger, "Role of extent of resection in the long-term outcome of low-grade hemispheric gliomas," J. Clin. Oncol. **26**(8), 1338–1345 (2008).
4. N. Sanai and M. S. Berger, "Glioma extent of resection and its impact on patient outcome," Neurosurgery **62**(4), 753–766 (2008).
5. I. Y. Eyüpoglu, M. Buchfelder, and N. E. Savaskan, "Surgical resection of malignant gliomas-role in optimizing patient outcome," Nat. Rev. Neurol. **9**(3), 141–151 (2013).
6. U. Pichlmeier, A. Bink, G. Schackert, and W. Stummer, "Resection and survival in glioblastoma multiforme: An RTOG recursive partitioning analysis of ALA study patients," Neuro-oncol. **10**(6), 1025–1034 (2008).
7. W. Stummer, J. C. Tonn, C. Goetz, W. Ullrich, H. Stepp, A. Bink, T. Pietsch, and U. Pichlmeier, "5-Aminolevulinic Acid-Derived Tumor Fluorescence: The Diagnostic Accuracy of Visible Fluorescence Qualities as Corroborated by Spectrometry and Histology and Postoperative Imaging," Neurosurgery **74**(3), 310–320 (2014).
8. Y. Li, R. Rey-Dios, D. W. Roberts, P. A. Valdés, and A. A. Cohen-Gadol, "Intraoperative Fluorescence-Guided Resection of High-Grade Gliomas: A Comparison of the Present Techniques and Evolution of Future Strategies," World. Neurosurg. **82**(1-2), 175–185 (2014).
9. T. Hollon, S. L. Hervey-Jumper, O. Sagher, and D. A. Orringer, "Advances in the Surgical Management of Low-Grade Glioma," Semin. Radiat. Oncol. **25**(3), 181–188 (2015).
10. A. Novotny, J. Xiang, W. Stummer, N. S. Teuscher, D. E. Smith, and R. F. Keep, "Mechanisms of 5-aminolevulinic acid uptake at the choroid plexus," J. Neurochem. **75**(1), 321–328 (2000).

#258145 Received 25 Jan 2016; revised 8 Mar 2016; accepted 12 Mar 2016; published 18 Apr 2016

11. M. Hefti, H. M. Mehdorn, I. Albert, and L. Dorner, "Fluorescence-Guided Surgery for Malignant Glioma: A Review on Aminolevulinic Acid Induced Protoporphyrin IX Photodynamic Diagnostic in Brain Tumors," Curr. Med. Imaging Rev. **6**(4), 254–258 (2010).
12. O. van Tellingen, B. Yetkin-Arik, M. C. de Gooijer, P. Wesseling, T. Wurdinger, and H. E. de Vries, "Overcoming the blood-brain tumor barrier for effective glioblastoma treatment," Drug Resist. Updat. **19**, 1–12 (2015).
13. C. Kut, K. L. Chaichana, J. Xi, S. M. Raza, X. Ye, E. R. McVeigh, F. J. Rodriguez, A. Quiñones-Hinojosa, and X. Li, "Detection of human brain cancer infiltration ex vivo and in vivo using quantitative optical coherence tomography," Sci. Transl. Med. **7**(292), ra100 (2015).
14. M. Ji, D. A. Orringer, C. W. Freudiger, S. Ramkissoon, X. Liu, D. Lau, A. J. Golby, I. Norton, M. Hayashi, N. Y. Agar, G. S. Young, C. Spino, S. Santagata, S. Camelo-Piragua, K. L. Ligon, O. Sagher, and X. S. Xie, "Rapid, label-free detection of brain tumors with stimulated Raman scattering microscopy," Sci. Transl. Med. **5**(201), 201ra119 (2013).
15. M. Ji, S. Lewis, S. Camelo-Piragua, S. H. Ramkissoon, M. Snuderl, S. Venneti, A. Fisher-Hubbard, M. Garrard, D. Fu, A. C. Wang, J. A. Heth, C. O. Maher, N. Sanai, T. D. Johnson, C. W. Freudiger, O. Sagher, X. S. Xie, and D. A. Orringer, "Detection of human brain tumor infiltration with quantitative stimulated Raman scattering microscopy," Sci. Transl. Med. **7**(309), 309ra163 (2015).
16. M. Jermyn, K. Mok, J. Mercier, J. Desroches, J. Pichette, K. Saint-Arnaud, L. Bernstein, M. C. Guiot, K. Petrecca, and F. Leblond, "Intraoperative brain cancer detection with Raman spectroscopy in humans," Sci. Transl. Med. **7**(274), ra19 (2015).
17. Y. Barad, H. Eisenberg, M. Horowitz, and Y. Silberberg, "Nonlinear scanning laser microscopy by third harmonic generation," Appl. Phys. Lett. **70**(8), 922–924 (1997).
18. M. Müller, J. Squier, K. R. Wilson, and G. J. Brakenhoff, "3D microscopy of transparent objects using third-harmonic generation," J. Microsc. **191**(3), 266–274 (1998).
19. J. Squier, M. Muller, G. Brakenhoff, and K. R. Wilson, "Third harmonic generation microscopy," Opt. Express **3**(9), 315–324 (1998).
20. D. Yelin and Y. Silberberg, "Laser scanning third-harmonic-generation microscopy in biology," Opt. Express **5**(8), 169–175 (1999).
21. J. X. Cheng and X. S. Xie, "Green's function formulation for third-harmonic generation microscopy," J. Opt. Soc. Am. B **19**(7), 1604–1610 (2002).
22. D. Oron, D. Yelin, E. Tal, S. Raz, R. Fachima, and Y. Silberberg, "Depth-resolved structural imaging by third-harmonic generation microscopy," J. Struct. Biol. **147**(1), 3–11 (2004).
23. D. Débarre and E. Beaurepaire, "Quantitative characterization of biological liquids for third-harmonic generation microscopy," Biophys. J. **92**(2), 603–612 (2007).
24. S. Witte, A. Negrean, J. C. Lodder, C. P. J. de Kock, G. Testa Silva, H. D. Mansvelder, and M. Louise Groot, "Label-free live brain imaging and targeted patching with third-harmonic generation microscopy," Proc. Natl. Acad. Sci. U.S.A. **108**(15), 5970–5975 (2011).
25. P. Mahou, N. Olivier, G. Labroille, L. Duloquin, J. M. Sintes, N. Peyriéras, R. Legouis, D. Débarre, and E. Beaurepaire, "Combined third-harmonic generation and four-wave mixing microscopy of tissues and embryos," Biomed. Opt. Express **2**(10), 2837–2849 (2011).
26. H. Lim, D. Sharoukhov, I. Kassim, Y. Zhang, J. L. Salzer, and C. V. Melendez-Vasquez, "Label-free imaging of Schwann cell myelination by third harmonic generation microscopy," Proc. Natl. Acad. Sci. USA **111**(50), 18025–18030 (2014).
27. G. J. Tserevelakis, E. V. Megalou, G. Filippidis, B. Petanidou, C. Fotakis, and N. Tavernarakis, "Label-free imaging of lipid depositions in C. elegans using third-harmonic generation microscopy," PLoS One **9**(1), e84431 (2014).
28. D. Débarre, W. Supatto, A. M. Pena, A. Fabre, T. Tordjmann, L. Combettes, M. C. Schanne-Klein, and E. Beaurepaire, "Imaging lipid bodies in cells and tissues using third-harmonic generation microscopy," Nat. Methods **3**(1), 47–53 (2006).
29. B. Weigelin, G.-J. Bakker, and P. Friedl, "Intravital third harmonic generation microscopy of collective melanoma cell invasion," IntraVital **1**(1), 32–43 (2012).
30. P. C. Wu, T. Y. Hsieh, Z. U. Tsai, and T. M. Liu, "In vivo quantification of the structural changes of collagens in a melanoma microenvironment with second and third harmonic generation microscopy," Sci. Rep. **5**, 8879 (2015).
31. J. Adur, V. B. Pelegati, A. A. de Thomaz, M. O. Baratti, D. B. Almeida, L. A. Andrade, F. Bottcher-Luiz, H. F. Carvalho, and C. L. Cesar, "Optical biomarkers of serous and mucinous human ovarian tumor assessed with nonlinear optics microscopies," PLoS One **7**(10), e47007 (2012).
32. N. Olivier, M. A. Luengo-Oroz, L. Duloquin, E. Faure, T. Savy, I. Veilleux, X. Solinas, D. Débarre, P. Bourgine, A. Santos, N. Peyriéras, and E. Beaurepaire, "Cell Lineage Reconstruction of Early Zebrafish Embryos Using Label-Free Nonlinear Microscopy," Science **329**(5994), 967–971 (2010).
33. S. Y. Chen, C. S. Hsieh, S. W. Chu, C. Y. Lin, C. Y. Ko, Y. C. Chen, H. J. Tsai, C. H. Hu, and C. K. Sun, "Noninvasive harmonics optical microscopy for long-term observation of embryonic nervous system development in vivo," J. Biomed. Opt. **11**(5), 054022 (2006).
34. G. Testa-Silva, M. B. Verhoog, N. A. Goriounova, A. Loebel, J. Hjorth, J. C. Baayen, C. P. J. de Kock, and H. D. Mansvelder, "Human synapses show a wide temporal window for spike-timing-dependent plasticity," Front. Synaptic Neurosci. **2**, 12 (2010).
35. O. Mărgăritescu, L. Mogoantă, I. Pirici, D. Pirici, D. Cernea, and C. Mărgăritescu, "Histopathological changes in acute ischemic stroke," Rom. J. Morphol. Embryol. **50**(3), 327–339 (2009).

#258145 Received 25 Jan 2016; revised 8 Mar 2016; accepted 12 Mar 2016; published 18 Apr 2016
(C) 2016 OSA

36. D. M. Huland, C. M. Brown, S. S. Howard, D. G. Ouzounov, I. Pavlova, K. Wang, D. R. Rivera, W. W. Webb, and C. Xu, "In vivo imaging of unstained tissues using long gradient index lens multiphoton endoscopic systems," Biomed. Opt. Express **3**(5), 1077–1085 (2012).
37. R. G. Liang, ed., *Biomedical Optical Imaging Technologies: Design and Applications*, Biological and Medical Physics, Biomedical Engineering (Springer, 2013), p. 382.
38. C. M. Brown, D. R. Rivera, I. Pavlova, D. G. Ouzounov, W. O. Williams, S. Mohanan, W. W. Webb, and C. Xu, "In vivo imaging of unstained tissues using a compact and flexible multiphoton microendoscope," J. Biomed. Opt. **17**(4), 040505 (2012).
39. H. Zeng, ed., *Diagnostic Endoscopy*, Series in Medical Physics and Biomedical Engineering (CRC Press, 2013).
40. R. Weigert, ed., *Advances in Intravital Microscopy: From Basic to Clinical Research*, Biomedical Sciences (Springer, 2014), p. 424.
41. D. R. Rivera, C. M. Brown, D. G. Ouzounov, I. Pavlova, D. Kobat, W. W. Webb, and C. Xu, "Compact and flexible raster scanning multiphoton endoscope capable of imaging unstained tissue," Proc. Natl. Acad. Sci. U.S.A. **108**(43), 17598–17603 (2011).
42. "Central Nervous System Histology Online Atlas", retrieved 2015, *http://141.214.65.171/Histology/Central%20Nervous%20System/view.apml*.
43. Z. X. Lin, "Glioma-related edema: new insight into molecular mechanisms and their clinical implications," Chin. J. Cancer **32**(1), 49–52 (2013).
44. A. Khanna, K. T. Kahle, B. P. Walcott, V. Gerzanich, and J. M. Simard, "Disruption of Ion Homeostasis in the Neurogliovascular Unit Underlies the Pathogenesis of Ischemic Cerebral Edema," Transl. Stroke Res. **5**(1), 3–16 (2014).
45. J. Duran and J. J. Guinovart, "Brain glycogen in health and disease," Mol. Aspects Med. **46**, 70–77 (2015).
46. N. G. Horton, K. Wang, D. Kobat, C. G. Clark, F. W. Wise, C. B. Schaffer, and C. Xu, "In vivo three-photon microscopy of subcortical structures within an intact mouse brain," Nat. Photonics **7**(3), 205–209 (2013).
47. J. P. Zinter and M. J. Levene, "Maximizing fluorescence collection efficiency in multiphoton microscopy," Opt. Express **19**(16), 15348–15362 (2011).
48. N. G. Horton, K. Wang, D. Kobat, C. G. Clark, F. W. Wise, C. B. Schaffer, and C. Xu, "In vivo three-photon microscopy of subcortical structures within an intact mouse brain," Nat. Photonics **7**(3), 205–209 (2013).
49. M. J. Levene, D. A. Dombeck, K. A. Kasischke, R. P. Molloy, and W. W. Webb, "In vivo multiphoton microscopy of deep brain tissue," J. Neurophysiol. **91**(4), 1908–1912 (2004).
50. T. A. Murray and M. J. Levene, "Singlet gradient index lens for deep in vivo multiphoton microscopy," J. Biomed. Opt. **17**(2), 021106 (2012).
51. D. R. Rivera, C. M. Brown, D. G. Ouzounov, I. Pavlova, D. Kobat, W. W. Webb, and C. Xu, "Compact and flexible raster scanning multiphoton endoscope capable of imaging unstained tissue," Proc. Natl. Acad. Sci. U.S.A. **108**(43), 17598–17603 (2011).
52. S.-H. Chia, C.-H. Yu, C.-H. Lin, N.-C. Cheng, T.-M. Liu, M.-C. Chan, I. H. Chen, and C.-K. Sun, "Miniaturized video-rate epi-third-harmonic-generation fiber-microscope," Opt. Express **18**(16), 17382–17391 (2010).
53. S. W. Chu, S. P. Tai, C. L. Ho, C. H. Lin, and C. K. Sun, "High-resolution simultaneous three-photon fluorescence and third-Harmonic-generation microscopy," Microsc. Res. Tech. **66**(4), 193–197 (2005).
54. D. M. Huland, M. Jain, D. G. Ouzounov, B. D. Robinson, D. S. Harya, M. M. Shevchuk, P. Singhal, C. Xu, and A. K. Tewari, "Multiphoton gradient index endoscopy for evaluation of diseased human prostatic tissue ex vivo," J. Biomed. Opt. **19**(11), 116011 (2014).
55. I. H. Chen, S. W. Chu, C. K. Sun, P. C. Cheng, and B. L. Lin, "Wavelength dependent damage in biological multi-photon confocal microscopy: A micro-spectroscopic comparison between femtosecond Ti:sapphire and Cr:forsterite laser sources," Opt. Quantum Electron. **34**(12), 1251–1266 (2002).
56. S. Y. Chen, H. Y. Wu, and C. K. Sun, "In vivo harmonic generation biopsy of human skin," J. Biomed. Opt. **14**(6), 060505 (2009).
57. J. M. Dela Cruz, J. D. McMullen, R. M. Williams, and W. R. Zipfel, "Feasibility of using multiphoton excited tissue autofluorescence for in vivo human histopathology," Biomed. Opt. Express **1**(5), 1320–1330 (2010).
58. G. Thomas, O. Nadiarnykh, J. van Voskuilen, C. L. Hoy, H. C. Gerritsen, and H. J. Sterenborg, "Estimating the risk of squamous cell cancer induction in skin following nonlinear optical imaging," J. Biophotonics **7**(7), 492–505 (2014).
59. F. S. Pavone and P. J. Campagnola, eds., *Second Harmonic Generation Imaging*, Series in Cellular and Clinical Imaging (CRC Press, 2013), Vol. 3, p. 476

1. Introduction

Glial tumors (gliomas) account for almost 80% of the tumors originating from brain tissue. The vast majority of these tumors are so-called 'diffuse gliomas' as they show very extensive ('diffuse') growth into the surrounding brain parenchyma. With surgical resection, irradiation, and/or chemotherapy it is impossible to eliminate all glioma cells without serious damage to the brain tissue. As a consequence, until now, patients with a diffuse glioma have had a poor prognosis, a situation which strongly contributes to the fact that brain tumor patients experience more years of life lost than patients with any other type of cancer [1,2].

Meanwhile it has also been demonstrated that the prognosis of patients with a diffuse glioma correlates with the extent of resection [3–5]. During brain surgery, however, it is

#258145 Received 25 Jan 2016; revised 8 Mar 2016; accepted 12 Mar 2016; published 18 Apr 2016
(C) 2016 OSA

extremely difficult for the neurosurgeon to determine the boundary of the tumor, i.e. whether a brain area contains tumor cells or not. If the neurosurgeon could have histopathological information on the tumor boundaries *during* brain surgery, then recognition of these tumor boundaries and with that, the surgical resection, could be significantly improved.

Occasionally, intra-operative analysis using hematoxylin-and-eosin (H&E) stained sections of snap-frozen material or smear preparations is performed by the pathologist to help establish brain tumor boundaries, but this procedure only allows analysis of small, selected regions, can only be performed on tissue fragments that are already resected, and is rather time consuming (frozen section diagnosis) or does not allow analysis of tumor in the histological context (smear preparations). Fluorescence imaging techniques are increasingly used during surgery [6,7] but are associated with several drawbacks, such as heterogeneous delivery and nonspecific staining [8,9]. In particular, low-grade gliomas and normal brain tissue have an intact blood-brain barrier and take up little circulating dye [10–12]. Alternative techniques are therefore required, that can detect the presence of tumor cells in tissue without fluorescent labels and with a speed that enables 'live' feedback to the surgeon while he/she operates.

The past year has seen exciting new developments in which optical coherence tomography [13] and stimulated Raman microscopy [14,15] were reported to reliably detect tumor tissue in the brain of human glioma patients, and a handheld Raman spectroscopy device was even implemented intra-surgical to assess brain tissue prior to excision [16]. These techniques are especially sensitive in densely tumor-infiltrated areas, and for the Raman spectroscopy device study a sensitivity limit of 17 tumor cells in an area of 150 × 150 μm^2 was reported. The discriminating power of the Raman techniques is based on subtle differences in the vibrational spectra of tumor tissue and healthy tissue, and they require extensive comparison of experimental spectra against libraries of reference spectra. A technique capable of directly visualizing the classical histopathological hallmark criteria currently used by pathologists for classification of tumor tissue could potentially be even more reliable and make the transition from the current practice—histopathological analysis of fixated tissue—to *in situ* optical biopsy easier. Diffuse gliomas are histopathologically characterized by variably increased cellularity, nuclear pleomorphism and—especially in higher-grade neoplasms—brisk mitotic activity, microvascular proliferation, and necrosis. To visualize these features in live tissue, a technique that elucidates the morphology of tissue is required. In this context, third harmonic generation (THG) microscopy is a promising tool because of its capacity to visualize almost the full morphology of tissue. THG is a nonlinear optical process that relies on spatial variations of the third-order non-linear susceptibility $\chi^{(3)}$ intrinsic to the tissue and (in the case of brain tissue) mainly arises from interfaces with lipid-rich molecules [17–27]. SHG signals arise from an optical nonlinear process involving non-centrosymmetric molecules present in, for example, microtubules and collagen. THG has been successfully applied to image unstained samples such as insect embryos, plant seeds and intact mammalian tissue [28], epithelial tissues [29–31], zebra fish embryos [32], and the zebra fish nervous system [33]. In brain tissue of mice, augmented by co-recording of SHG signals, THG was shown to visualize cells, nuclei, the inner and outer contours of axons, blood cells, and vessels, resulting in the visualization of both gray and white matter (GM and WM) as well as vascularization, up to a depth of 350 μm [24,26]. Here, we explore the potential of THG and SHG imaging for real time analysis of *ex-vivo* human brain tissue in the challenging cases of diffuse tumor invasion in low-grade brain tumors as well as of high-grade gliomas and structurally normal brain tissues.

2. Materials and methods

2.1 Tissue processing

Structurally normal brain samples were cut from the temporal cortex and subcortical white matter that had to be removed for the surgical treatment of deeper brain structures for epilepsy. Tumor brain samples were cut from tumor margin areas (especially in low-grade

#258145 Received 25 Jan 2016; revised 8 Mar 2016; accepted 12 Mar 2016; published 18 Apr 2016
(C) 2016 OSA

diffuse glioma cases) and from the tumor core and peritumoral areas (in high-grade glioma cases). After resection, the brain tissue samples were placed within 30 s in ice-cold artificial cerebrospinal fluid (ACSF) at 4°C containing (in mM): NaCl (125); KCl (3); NaH_2PO_4 (1.25); $MgSO_4$ (2); $CaCl_2$ (2); $NaHCO_3$ (26); glucose (10); with an osmolarity of 300 mosmol/kg [34]; and transported to the laboratory, located within a distance of 200 m from the operating room. The transition time between resection of the tissue and the start of preparing slices was less than 15 min. We prepared a 300–350 μm thick coronal slice of the freshly-excised structurally normal tissue in ice-cold ACSF solution with a vibratome (Microm, HM 650V, Thermo Fisher Scientific). The slice was then placed in a plastic Petri dish (diameter 50 mm) and covered with a 0.17 mm thick glass cover slip to provide a flat sample surface during multiphoton imaging. Freshly-excised tumor tissue samples were cut with a surgical scalpel in several individual slices to generate flat surfaces, rinsed with ACSF to remove blood contamination, embedded in 20 × 20 × 5 mm^3 agar blocks (40 mg/mL water solution of OXOID bacteriological agar, LP0011) and flattened with thin glass cover slips (0.17 mm thick, dia. 25 mm, Menzel-Gläser). All procedures on human tissue were performed with the approval of the Medical Ethical Committee of the VU University Medical Center and in accordance with Dutch license procedures and the declaration of Helsinki. All patients gave a written informed consent for tissue biopsy collection and signed a declaration permitting the use of their biopsy specimens in scientific research.

2.2 Tissue histology

After THG/SHG imaging, brain tumor samples were fixated in 4% formaldehyde, embedded in paraffin, sliced in 5-μm-thick histological sections and routinely stained with hematoxylin and eosin (H&E) and luxol fast blue (LFB) for microscopic examination. Low- and high-magnification images were obtained using a Leica DM4000B microscope, equipped with a Leica digital camera (Leica DC500). Images were recorded and stored using IM50 imaging software and processed with ImageJ software (ver. 1.49m, NIH, USA). LFB images of structurally normal human cortex were acquired from the online Central Nervous System Histology Atlas [35].

2.3 Multiphoton imaging

THG and SHG are nonlinear optical processes that may occur in tissue depending on the nonlinear susceptibility coefficients $\chi^{(3)}$ and $\chi^{(2)}$ of the tissue and upon satisfying phase matching conditions [17–19,21,23–27]. In the THG process, three incident photons are converted into one photon with triple energy and one third of the wavelength (Fig. 1(A)). In the SHG process, signals result from the conversion of an incident photon pair into one photon with twice the energy and half the wavelength. Two- and three photon excited fluorescence signals (2PF, 3PF) may simultaneously be generated by intrinsic proteins (Fig. 1(B)). As a result, a set of distinct (harmonic) and broadband (autofluorescence) spectral peaks is generated in the visible range. The imaging setup (Fig. 1(C)) to generate and collect these signals consisted of a commercial two-photon laser-scanning microscope (TriMScope I, LaVision BioTec GmbH) and a femtosecond laser source. The laser source was an optical parametric oscillator (Mira-OPO, APE) pumped at 810 nm by a Ti-sapphire oscillator (Coherent Chameleon Ultra II). The OPO generates 200 fs pulses at 1200 nm with a repetition rate of 80 MHz. We selected this wavelength as it falls in the tissue transparency window, providing deeper penetration and reduced photodamage compared to the 700–1000 nm range, as well as harmonic signals generated in the visible wavelength range, facilitating their collection and detection with conventional objectives and detectors. We focused the OPO beam on the sample using a 25 × /1.10 (Nikon APO LWD) water-dipping objective (MO). The 1200 nm beam focal spot size on the sample was $d_{lateral}$ ~0.7 μm and d_{axial} ~4.1 μm. It was measured with 0.175 μm fluorescent microspheres (see Section 3.4) yielding two- and three-photon resolution values $\Delta_{2P,lateral}$ ~0.5 μm, $\Delta_{2P,axial}$ ~2.9 μm, $\Delta_{3P,lateral}$ ~0.4 μm, and $\Delta_{3P,axial}$ ~2.4 μm. Two high-sensitivity GaAsP photomultiplier tubes (PMT, Hamamatsu H7422-40) equipped with narrowband filters at 400 nm and 600 nm were used to collect the THG and

#258145 Received 25 Jan 2016; revised 8 Mar 2016; accepted 12 Mar 2016; published 18 Apr 2016
(C) 2016 OSA

SHG signals, respectively, as a function of position of the focus in the sample. The signals were filtered from the 1200 nm fundamental photons by a dichroic mirror (Chroma T800LPXRXT, DM1), split into SHG and THG channels by a dichroic mirror (Chroma T425LPXR, DM2), and passed through narrow-band interference filters (F) for SHG (Chroma D600/10X) and THG (Chroma Z400/10X) detection. The efficient back-scattering of the harmonic signals allowed for their detection in epi-direction. The laser beam was transversely scanned over the sample by a pair of galvo mirrors (GM). THG and SHG modalities are intrinsically confocal and therefore provide direct depth sectioning. We obtained a full 3D image of the tissue volume by scanning the microscope objective with a stepper motor in the vertical (z) direction. The mosaic imaging of the sample was performed by transverse (xy) scanning of the motorized translation stage. Imaging data was acquired with the TriMScope I software ("Imspector Pro"); image stacks were stored in 16-bit tiff-format and further processed and analyzed with "ImageJ" software (ver. 1.49m, NIH, USA). All images were processed with logarithmic contrast enhancement.

2.4 Endomicroscopy imaging

For endomicroscopic imaging we used a commercial high-numerical-aperture (NA) multi-element micro-objective lens (GT-MO-080-018-810, GRINTECH) composed of a plano-convex lens and two GRaded INdex (GRIN) lenses with aberration compensation, object NA = 0.80 and object working distance 200 µm (in water), image NA = 0.18 and image working distance 200 µm (in air), magnification × 4.8 and field-of-view diameter of 200 µm. The GRIN lenses and the plano-convex lens were mounted in a waterproof stainless steel housing with an outer diameter of 1.4 mm and a total length of 7.5 mm. Originally designed for a wavelength range of 800–900 nm [36–41], this micro-objective lens was used for focusing of 1200 nm femtosecond pulses and collection of back-scattered harmonic and fluorescence photons. A coupling lens with f = 40 mm (NA = 0.19, Qioptiq, ARB2 NIR, dia. 25 mm) focused the scanned laser beam in the image plane of the micro-objective lens and forwarded the epi-detected harmonic and fluorescence photons to the PMTs.

We characterized the lateral (x) and axial (z) resolution of the micro-objective lens by 3D imaging of fluorescence microspheres (PS-Speck Microscope Point Source Kit, P7220, Molecular Probes). We used "blue" and "deep red" microspheres, 0.175 ± 0.005 µm in diameter, with excitation/emission maxima at 360/440 nm and 630/660 nm to obtain three-photon (3P) and two-photon (2P) point spread function (PSF) profiles. The excitation wavelength was 1200 nm, and fluorescence signals were detected in the 400 ± 5 nm (3P) and 600 ± 5 nm (2P) spectral windows, just as in the brain tissue imaging experiments. 1 µL of "blue" and "deep red" sphere suspensions were applied to a propanol-cleaned 75 × 26 × 1 mm^3 glass slide. The mixed microsphere suspension was left to dry for 20 min and was then imaged with the micro-objective lens via a water immersion layer. The assembly of the coupling lens and the micro-objective lens was vertically (z) scanned with a step of 0.5 µm, and stacks of two-/three-photon images were recorded. The line profiles were then taken over the lateral (xy) images of the fluorescent spheres with maximal intensity (in focus), and fluorescence counts were plotted as function of the lateral coordinate (x). The axial (z) scan values of the two- and three-photon fluorescence signals were acquired by averaging of the total fluorescence counts of the corresponding spheres and were plotted as function of the axial coordinate (z). Lateral (x) and axial (z) 2P/3P points were then fitted with Gaussian functions and full width at half-maximum (FWHM) values were measured.

3. Results

3.1 THG/SHG microscopy of structurally normal human brain tissue

We imaged brain tissue samples from eight patients diagnosed with low-grade glioma and two patients diagnosed with high-grade glioma, as well as one structurally normal reference with THG/SHG microscopy, and compared the images with the histology of these samples. We used near-infrared laser pulses with a central wavelength of 1200 nm and a duration of 200

#258145 Received 25 Jan 2016; revised 8 Mar 2016; accepted 12 Mar 2016; published 18 Apr 2016
(C) 2016 OSA

femtoseconds to generate second and third harmonic photons from the brain tissue structures at 600 and 400 nm respectively; see Fig. 1(A)–1(D). In all images, the THG signals collected at 400 nm are depicted in green, and the signals collected at 600 nm are depicted in red. Where the signals overlap, they result in yellow color. Tissue samples, obtained with consent from the patients, were all imaged without further preparation steps, apart from one dissection to generate a flat surface. Figures 1(E), 1(F) show freshly excised tumor tissue samples of low- (Fig. 1(E)) and high-grade (Fig. 1(F)) glioma cases and an agar-embedded tumor tissue sample under the multiphoton microscope (Fig. 1(G)).

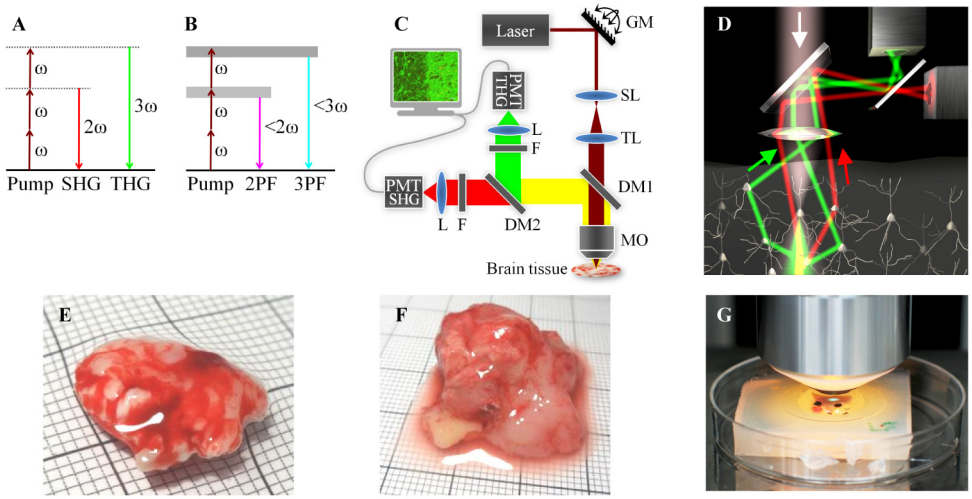

Fig. 1. THG/SHG microscopy for brain tissue imaging. (A) Energy level diagram of the second (SHG) and third (THG) harmonic generation process. (B) Energy level diagram of the two- (2PF) and three-photon (3PF) excited auto-fluorescence process. (C) Multiphoton microscope setup: Laser producing 200 fs pulses at 1200 nm; GM – X-Y galvo-scanner mirrors; SL – scan lens; TL – tube lens; MO – microscope objective; DM1 – dichroic mirror reflecting back-scattered THG/SHG photons to the PMT detectors; DM2 – dichroic mirror splitting SHG and THG channels; F – narrow-band SHG and THG interference filters; L – focusing lenses; PMT – photomultiplier tube detectors. (D) Infrared photons (white arrow) are focused deep in the brain tissue, converted to THG (green) and SHG (red) photons, scattered back (green/red arrows) and epi-detected. The nonlinear optical processes result in label-free contrast images with sub-cellular resolution and intrinsic depth sectioning. (E and F) Freshly-excised low-grade (E) and high-grade (F) glioma tissue samples in artificial cerebrospinal fluid (ACSF) in a Petri dish with a millimeter paper underneath for scale. (G) An agar-embedded tumor tissue sample under 0.17 mm glass cover slip with the microscope objective (MO) on top.

We started with imaging of freshly excised, unfixed, structurally normal, human brain tissue samples (neocortex/GM and subcortical WM) from a patient undergoing lobectomy for intractable epilepsy. The images obtained from these tissues were used to provide 'healthy reference' THG/SHG images. Figure 2(A) shows a combined mosaic THG/SHG image of brain tissue sliced perpendicular to the brain surface with a transition from neocortex (top) to WM (bottom), Figs. 2(C), 2(E), 2(G), 2(I) show higher magnifications of selected areas (marked in Fig. 2(A) with white squares). White dotted lines delineate individual 'tiles' composing the full 'mosaic' image. Figure 2(A) reveals the neuropil (i.e. the dense network of neuronal and glial cell processes) with neuronal/glial cell somata (Fig. 2(C), 2(E), 2(G)), dispersed microvessels with multiple intraluminal erythrocytes (Fig. 2(I)), and—especially in the WM—many lipid-rich, myelinated axons. Some of the neuronal somata are filled with lipofuscin granules, emitting in both THG and SHG channels and therefore appearing yellow (Fig. 2(E)). The transition between the neocortex (top) and lipid-rich WM (bottom) is clearly visualized, revealing somata of glial cells appearing as dark 'holes' in the bright neuropil matrix (Fig. 2(G)), with round nuclei and occasional nucleoli. The information in the THG/SHG images is very similar to that observed in the on-line brain atlas images of

#258145 Received 25 Jan 2016; revised 8 Mar 2016; accepted 12 Mar 2016; published 18 Apr 2016
(C) 2016 OSA

histological sections (Fig. 2(B), 2(D), 2(F), 2(H), 2(J)) of similar tissue areas, with luxol fast blue (LFB) staining to demonstrate myelin in Fig. 2(B), 2(D), 2(F), 2(H) and H&E staining in Fig. 2(J) [42]. Visualization 1, Visualization 2, and Visualization 3 show scans over a depth of 0–50 µm below the tissue surface of the areas depicted in Fig. 2(C), 2(E), 2(G).

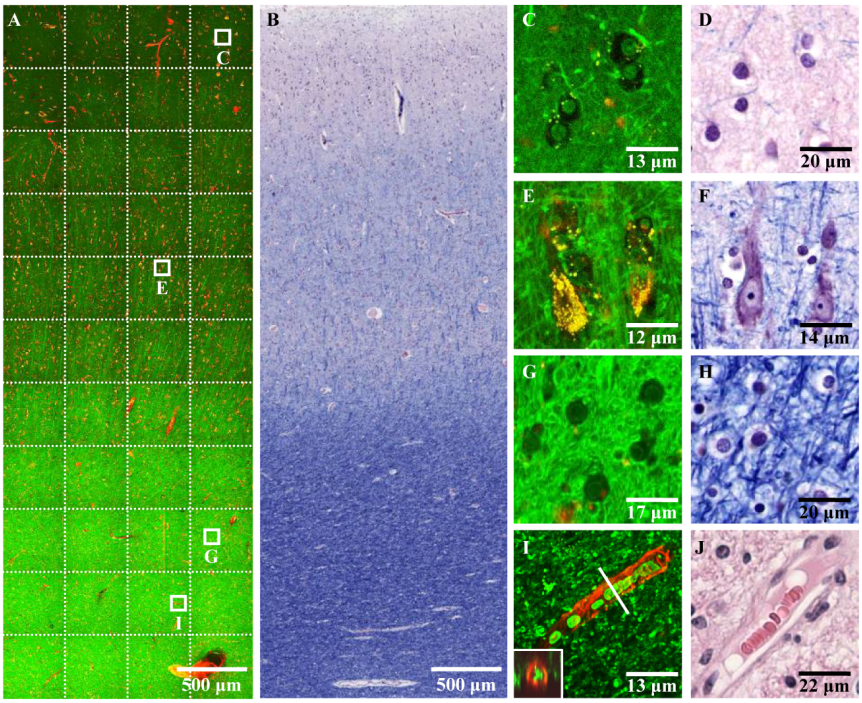

Fig. 2. Structurally normal human brain tissue. (A) THG (green) and SHG (red) image of 1.80 × 4.95 mm^2 *ex-vivo*, structurally normal, fresh human neocortex and subcortical white matter tissue. (B) Myelin-stained histology image of a similar region of the brain. Key tissue components marked with white squares are shown enlarged in the right panels, together with histology images; molecular layer (C, D); large pyramidal neurons layer (E, F); white matter (G, H); a capillary blood vessel with intraluminal erythrocytes (I, J). The stain in panels (B, D, F, H) is luxol fast blue (LFB) to reveal myelin, and hemotoxin-and-eosion (H&E) in (J). Images C, E and G are composed of single 2-µm-thick optical sections, imaging time 1.2 s. Image I is composed of 21 images taken with 2-µm steps over 40 µm depth, imaging time 1.5 min. The inset of image I shows a cross-section of the capillary along the white line, revealing a round contour of this microvessel (SHG) and corroborating the intraluminal position of the erythrocytes (THG).

3.2 THG/SHG imaging of human brain tumor tissues

Diffuse gliomas are histopathologically characterized by variably increased cellularity, nuclear pleomorphism, and—especially in higher-grade neoplasms—brisk mitotic activity, microvascular proliferation, and necrosis. In routine histopathological examination of the transition zone of a diffuse glioma in normal brain tissue, increased cellularity with concomitant rarefaction of the neuropil and—especially in the high-grade malignant cases—nuclear pleomorphism are used for discriminating normal from abnormal tissue. To identify such tumor-invaded zones in the brain tissue samples, which typically had an area of 10 × 10 mm^2, we used a rapid 2D-THG inspection mode. Visualization 4 and Visualization 5 show in real-time the videos recorded while XYZ-scanning the sample under the microscope, which typically took less than 60 seconds. We performed detailed 3D imaging in areas where variations in the density of cells and of the white matter were observed. Figure 3(A) shows a large field-of-view mosaic image where THG intensity increases from right to left. Upon magnification of the areas marked in Fig. 3(A), it becomes clear that the low THG intensity in

#258145 Received 25 Jan 2016; revised 8 Mar 2016; accepted 12 Mar 2016; published 18 Apr 2016
(C) 2016 OSA

the right part is due to an abnormally high density of cells in the WM, combined with rarefaction of the neuropil. Based on these two criteria, in an H&E image this tissue would be labeled as very typical of diffuse glioma infiltration. The tumor cells can be clearly recognized in Fig. 3(C), 3(D), including intracellular details such as the nuclei and nucleoli of the tumor cells. After THG imaging, we fixated and stained the tissue with H&E and examined histological sections. One-to-one comparison of the sections with THG images proved difficult because of the distortions of the tissue in the fixation process. However, parts of the sections cut from the volume analyzed with THG demonstrate a similar increase in cell density by the H&E staining (Fig. 3(E)–3(H)), which served as definitive proof of the presence of diffuse low-grade glioma in this area. Visualization 6 and Visualization 7 show 3D depth scans corresponding to Fig. 3(C), 3(D), that reveal tumor-invaded areas in deeper layers of the tissue.

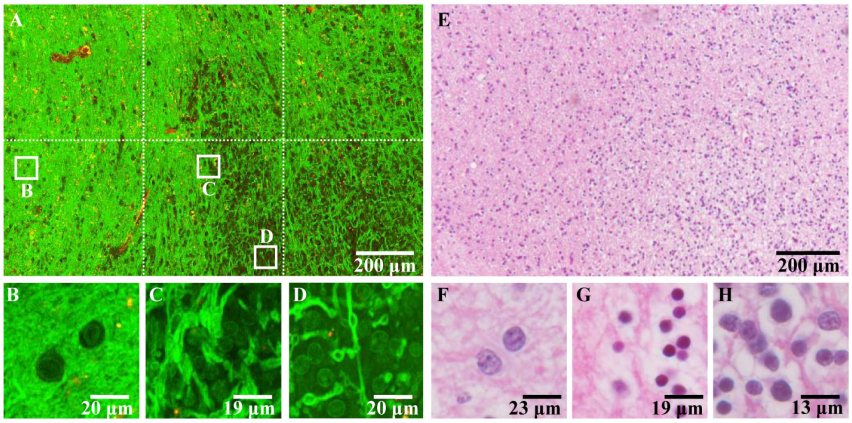

Fig. 3. Infiltrative low-grade glioma: transition zone. (A–D) THG/SHG images of the low-to-high cellularity transition zone in a tissue sample diagnosed by the neuropathologist as diffuse low-grade oligodendroglioma on the basis of H&E-stained histological sections. (A) Mosaic image of the transition zone in the white matter. Image is composed of 3 × 2 = 6 tiles, 1.35 × 0.90 mm^2, each tile 450 × 450 μm^2, 1000 × 1000 $pixels^2$, total imaging time 52 sec. (B–D) Magnified low- (B), intermediate- (C) and high-cellularity (D) areas marked on the image (A) with white squares. Images (B, C) show 2-µm-thick optical sections taken at depths of 20–30 µm with acquisition time of 0.6 s. (E to H) H&E images of the sample areas corresponding to the THG/SHG images: A–E, B–F, C–G, D–H.

Figure 4 shows an example of WM brain tissue where mixed areas of high and low cellularity were observed in the case of a patient diagnosed with infiltrative low-grade glioma. The THG images resolve the corresponding increased cell densities due to the presence of tumor cells in the WM, in the large image by the lower THG signals, and in the smaller field-of-view images by the contours outlining individual cells, nuclei and nucleoli. The SHG signals visualize small blood vessels in the tissue, and yellow, probably fluorescent, deposits are observed throughout the tissue. The imaging time of the full area of 4.4 × 3.2 mm^2, recorded with sub-cellular resolution, was 5 minutes.

#258145 Received 25 Jan 2016; revised 8 Mar 2016; accepted 12 Mar 2016; published 18 Apr 2016
(C) 2016 OSA

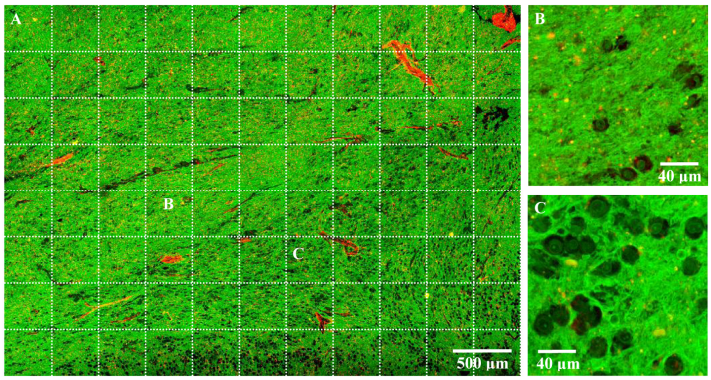

Fig. 4. Infiltrative low-grade glioma: mixed cellularity area. (A) Mosaic image of brain tumor area with spatially varying cellular density. Image is composed of single images (tiles) with boundaries indicated by dotted white lines, each tile is 400 × 400 µm^2, 254 × 254 pixels^2. Each tile shows a single optical section about 2-µm thick and taken at a depth of 20–30 µm. Mosaic size: 11 × 8 = 88 tiles; imaged area: 4.4 × 3.2 mm^2; total imaging time: 3.7 min. (B,C) Magnified images of the low- (B) and increased cellularity (C) areas indicated on the image (A). Images (B,C) show single optical sections about 2-µm thick taken at depths of 20–30 µm with an acquisition time of 5 s.

To illustrate the difference with low-grade glioma tissue, in Fig. 5 we show an image of high-grade glioma tissue, taken from the core of a tumor in the WM. Here, the axon matrix has completely disappeared and the entire volume is filled with tumor cells. The SHG signals from the collagen of the vessel walls visualize the dramatically increased vascularization typical for tumor cores, to satisfy the increased need for oxygen due to the high metabolic rate of tumor cells. The smaller blood vessel in Fig. 5(B) contains some individual erythrocytes.

Figure 6 shows an image of neocortex tissue from a patient diagnosed with high-grade glioma. The secondary effects of the high-grade glioma on the surrounding neocortical tissue could be recognized by our expert pathologist PW. Figure 6(A) shows bright cells, vessels and, in the lower left, a tumor cell lesion. The bright appearance of the neuronal/glial cells may arise from tumor-induced edema. Tumor-induced edema [43] of peritumoral neocortex tissue results in disruption of ion homeostasis in neuronal and glial cells [44] and leads to increased uptake of extracellular fluid by cellular somata, cytoplasmic swelling, and formation of intracellular vacuoles. Multiple inter-vacuolar interfaces may be the source of the strong third harmonic signal and result in the bright appearance of the vacuolated cells.

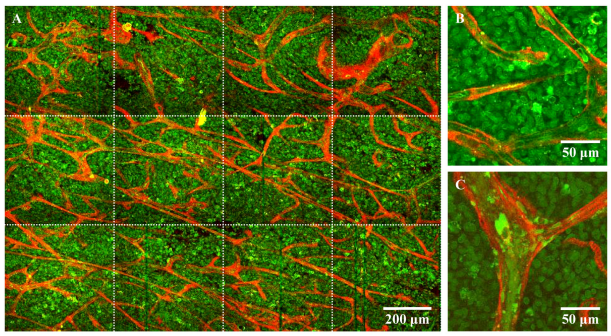

Fig. 5. High-grade glioma in the white matter. Combined THG/SHG images of the focus of a high-grade glioma with high cellularity and intense vascular proliferation. (A) Mosaic image composed of single tiles, each tile 450 × 450 µm^2, 517 × 517 pixels^2, each tile showing a single 2-µm-thick optical section taken at a depth of 20–30 µm. Mosaic size 4 × 3 = 24 tiles; imaged area 1.80 × 1.35 mm^2; total imaging time 1.5 min. (B and C) Magnified images of the areas containing smaller (B) and larger (C) blood vessels. Images (B and C) show single 2-µm-thick optical sections taken at depths of 20–30 µm with an acquisition time of 8 s. H&E histology of the HGG sample is shown in Fig. 7.

#258145 Received 25 Jan 2016; revised 8 Mar 2016; accepted 12 Mar 2016; published 18 Apr 2016
(C) 2016 OSA

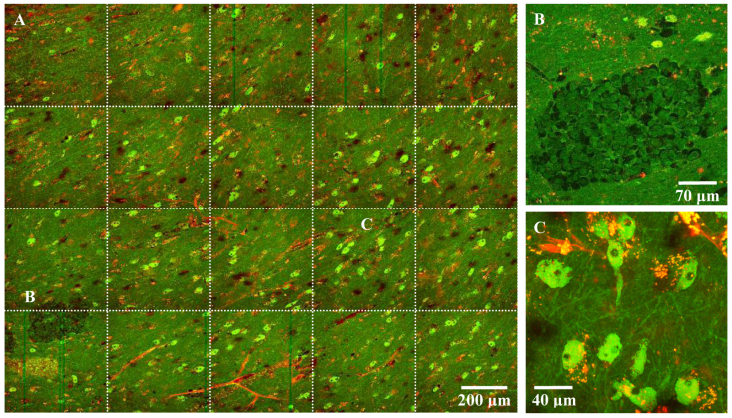

Fig. 6. High-grade glioma: peritumoral neocortex tissue with secondary changes. (A) Mosaic image is composed of 450 × 450 µm^2 tiles, 517 × 517 pixels^2, each tile showing a single 2-µm-thick optical section taken at a depth of 20–30 µm. Mosaic size 5 × 4 = 20 tiles; imaged area 2.25 × 1.80 mm^2; total imaging time 1.7 min. (B and C) Magnified image of a tumor cell lesion (B) and an area with bright cells (black round holes are cells' nuclei) and a blood vessel (C). Images (B and C) show single 2-µm-thick optical sections taken at depths of 20–30 µm, acquisition times 15 s (B) and 8 s (C).

Figure 7 shows examples of different phenotypes of cells that were observed with THG/SHG imaging in the low- and high-grade glioma samples. Nuclei and nucleoli of glial and tumor cells were observed, as shown in the examples above, but also cytoplasm of vacuolated cells, the dense hyaline mass of *corpus amylaceum* (a proteinaceous product of glial cells [45]), and autofluorescent deposits in the neuropil. For each cell type, we found an almost perfect match in the H&E histological images, allowing for identification of most of these elements. Clearly, the THG images allow for the characterization of relevant pathological parameters such as nucleus-to-cytoplasm ratio (Fig. 7(A)–7(D)) and the pleomorphism of tumor cells (Fig. 7(G)).

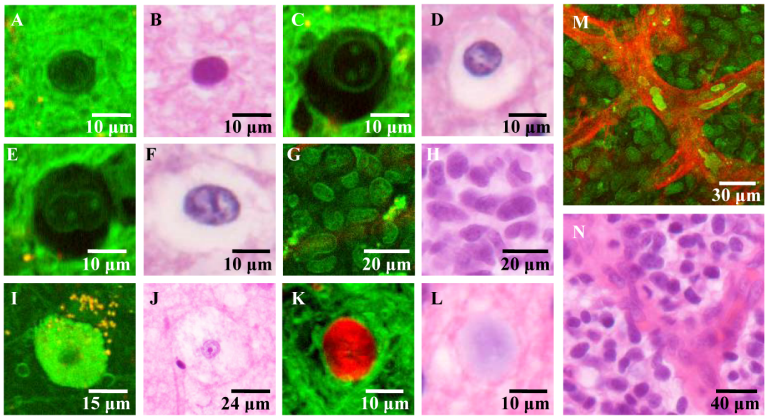

Fig. 7. Various cytological and histological features observed with THG/SHG imaging modalities in low- and high-grade glioma tissues. Label-free images of 2-µm-thick optical sections taken at depths of 20–30 µm with acquisition times of 0.5–5 s and H&E images of corresponding tissue areas. (A, B) Glial cell with a nearly round nucleus and large nuclear/cytoplasm ratio. (C, D) Glial cell with a round nucleus and smaller nuclear/cytoplasm ratio. (E, F) Glial cell with an indented nucleus and multiple nucleoli. (G, H) Highly cellular area in high-grade glioma (glioblastoma) with multiple pleomorphic tumor cell nuclei with dense chromatin and high nuclear/cytoplasmatic ratio. (I, J) A neuronal or glial cell with vacuolated cytoplasm in the edematic peritumoral neocortex of the high-grade glioma tissue. Autofluorescent deposits in the neuropil appear as yellow dots. (K, L) *Corpus amylaceum* surrounded by neuropil. (M, N) Intense vascular proliferation in high-grade glioma focus.

#258145 Received 25 Jan 2016; revised 8 Mar 2016; accepted 12 Mar 2016; published 18 Apr 2016
(C) 2016 OSA

In Table 1 we give a summary of the cases we investigated, with the pre-operative diagnosis, the features observed in the THG/SHG images, and the pathological hallmarks observed after histopathological analysis of the tissue. For each case, the pathologically relevant morphological features observed in the H&E images were also observed in the THG/SHG images.

Table 1. Pre-operative diagnoses and cell densities observed in the studied brain tissue samples by THG imaging and corresponding H&E histopathology.

#	Pre-operative diagnosis	THG	H&E
1	Left-frontal diffuse astrocytoma	Transition from normal to increased cell density	Transition from normal to increased cell density
2	Focally anaplastic diffuse glioma	Transition from normal to increased cell density	Transition from normal to increased cell density
3	Left fronto-parietal oligo-astrocytoma	Transition from normal to high cell density (Fig. 4)	Transition from normal to high cell density
4	Right parietal low-grade oligo-astrocytoma	Normal cell density	Normal cell density
5	Left parietal low-grade oligodendroglioma	Transition from normal to high cell density (Fig. 3(A)–3(D), Visualization 4, Visualization 6, Visualization 7)	Transition from normal to high cell density (Fig. 3(E)–3(H))
6	Right insular low-grade oligodendroglioma	Regions with increased cell density, regions with high cell density	Regions with increased cell density, regions with high cell density
7	Left-frontal low-grade glioma.	Normal cell density and transition from normal to high cell density	Normal cell density and transition from normal to high cell density
8	Temporoinsular low-grade glioma	Normal cell density	Normal cell density
9	High-grade glioma (glioblastoma)	Tumor core with high cell density (Fig. 5, Fig. 7(G), 7(M); Visualization 5)	Tumor core with high cell density (Fig. 7(H), 7(N))
10	High-grade glioma (glioblastoma)	Peritumoral tissue with vacuolated cells (Figs. 6, 7(I))	Peritumoral tissue with vacuolated cells (Fig. 7(J))

3.3 Imaging depth of THG as a function of tissue composition

An important advantage of THG/SHG imaging is that volumes of tissue can be imaged. The penetration depth at a given excitation wavelength and for a given NA is strongly dependent on the type of tissue. To characterize the penetration depth in different brain tissues, we first looked with more detail at the THG signal intensities generated by the different types of brain tissue, i.e. WM, GM, and tumor-invaded tissue. Figure 2(A) clearly shows that the WM areas of the brain generate a stronger THG signal than the GM. In Fig. 8(A) and 8(B) we quantified this to be a factor of 4, for a measurement taken at a depth of 20 μm, and a factor of 7 when measured closer to the surface of the tissue. Tumor-invasion in the WM in a low-grade glioma with low and high cell densities and in a high-grade glioma area (denoted as T1, T2 and T3, respectively), all lead to lower THG signals, Fig. 8(B).

Then, for each tissue type, we measured the decrease in signal intensity upon translation of the focus deeper into the tissue. We fitted the resulting intensity profile to an exponential decay, $I_{THG}(z) = I(0)\exp(-z/l_e)$ to obtain the effective attenuation length l_e, which has two separate contributions: absorption in tissue (water), l_a, and tissue scattering l_s with $l_e = (1/l_a + 1/l_s)^{-1}$; l_a and l_s are each dependent on wavelength. For example, at 1200 nm wavelength the impact of scattering is larger (smaller l_s) and water absorption is smaller (larger l_a) compared to 1700 nm where water absorption is higher and scattering smaller [46]. The value of l_e is

#258145 Received 25 Jan 2016; revised 8 Mar 2016; accepted 12 Mar 2016; published 18 Apr 2016
(C) 2016 OSA

maximum for areas with low axon fiber densities: GM and T3 (l_e = 52 μm) and decreases by factor 4 for WM and T1 (l_e = 13 μm). Cells and fibers can be distinguished down to $z_{max} = 3l_e$. Maximum THG imaging depth z_{max} for human brain tissues is then 40–150 μm in the current study for a wavelength of 1200 nm and an NA = 1.1. The THG effective attenuation length l_e is dependent on the tumor cell density, tumor-induced changes to the pre-existent tissue architecture, and the tissue type (GM or WM). Earlier we reported a penetration depth of z_{max} > 300 μm in the cortex of young mouse brain [24] while here we show that scattering properties of human tissue result in smaller effective attenuation length. Using fully optimized detection systems, penetration depths of 850 mm for 2-photon fluorescence in mouse cortex [47], and 1.4 mm for 3-photon fluorescence at 1700 nm in mouse cortex [48] have been achieved.

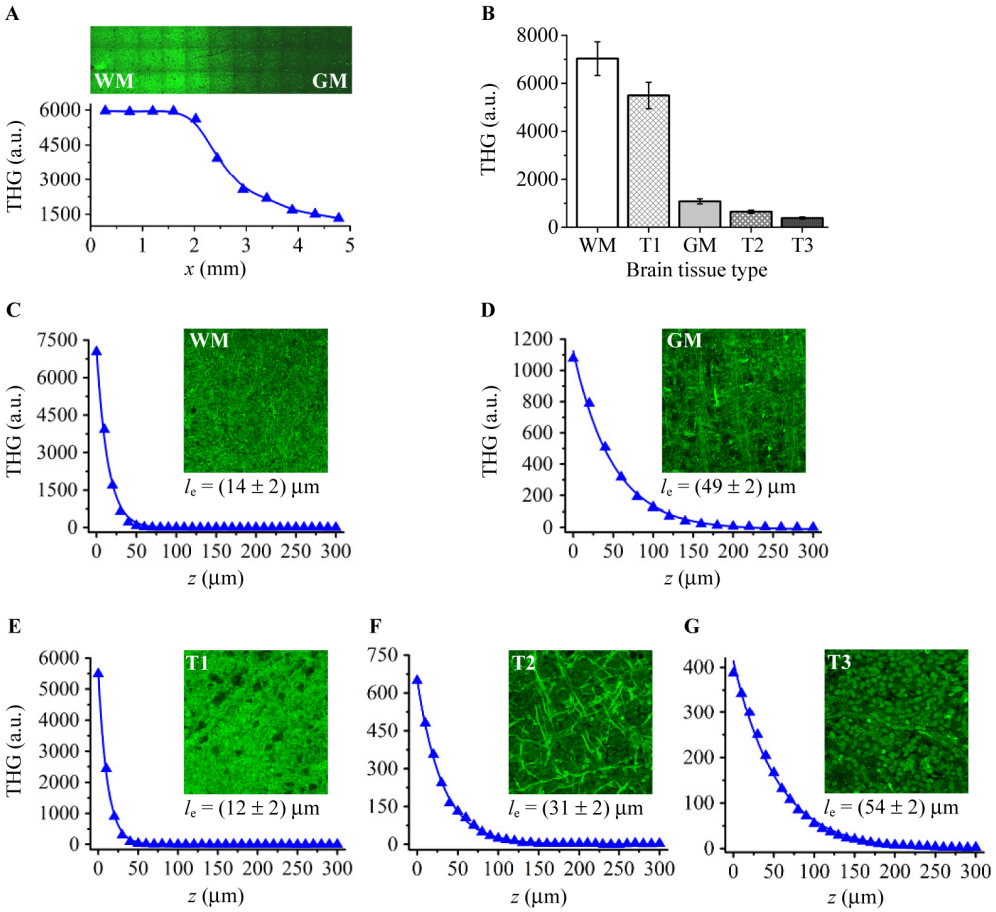

Fig. 8. THG imaging for different brain tissues types at varying depths. (A) Horizontal THG intensity profile was taken over a mosaic image of a white-to-gray matter transition of structurally normal human brain tissue. The mosaic was imaged at a depth of 10–20 μm. As the myelinated fiber density increases from gray matter (GM) to white matter (WM), the THG signal intensity increases by a factor 4. (B) Histogram showing averaged THG signal intensities obtained from THG images collected at depths of 2–4 μm from structurally normal brain WM and GM areas, compared to low-grade glioma areas of WM with low (T1) and high (T2) cell densities and high-grade glioma area (T3) with high cell density. Overall, THG signal intensity increases by factor 17 from T3 to WM. (C to G) THG intensity depth profiles of WM, GM, T1, T2 and T3 areas. THG intensity points (triangles) are obtained by averaging 270 × 270 μm^2 images taken every 10 μm down to 300 μm. Solid lines present exponential decay fits: $I_{THG}(z) = I(0) \exp(-z/l_e)$, where l_e denotes the THG effective attenuation length, $I_{THG}(l_e) = 0.37\, I_{THG}(0)$.

#258145 Received 25 Jan 2016; revised 8 Mar 2016; accepted 12 Mar 2016; published 18 Apr 2016
(C) 2016 OSA

3.4 Brain tumor THG/SHG microendoscopy

The results presented above demonstrate fast, *ex-vivo*, analysis of brain tissue with THG of histopathological quality. The ultimate goal is, however, to guide the neurosurgeon by *in situ* pathological analysis of the tumor boundaries, i.e. before the brain tissue is resected. With a handheld bioptic needle employing THG/SHG modalities, a neurosurgeon would be able to take 'optical biopsies' directly in the brain that is being operated on, imaging underlying tissue layers to decide whether to remove or spare the inspected tissue areas. THG and SHG imaging modalities require only a single laser beam, and allow for relatively high-speed imaging of backscattered photons, which makes them particularly suitable for incorporation into a handheld bioptic needle. Multi-photon imaging modalities including SHG and THG have been successfully miniaturized into micro-endoscopic multi-photon imaging devices enabling *in situ* analysis of tissue [38,49–54]. The images discussed above were measured with NA = 1.1. Such high NAs are not available for micro-objectives; therefore, much lower THG signal intensities are expected because the THG signal intensity scales as the 6th power of the NA. Here, we demonstrate that *ex-vivo* human brain tissue images similar to those obtained using our normal microscope can be obtained using a 7.5 mm long THG/SHG bioptic needle. We used a commercial high-NA multi-element micro-objective lens composed of a plano-convex lens and two GRIN lenses with aberration compensation, object NA = 0.80 and object working distance 200 μm (in water), image NA = 0.18 and image working distance 200 μm (in air), magnification × 4.8 and field of view diameter of 200 μm. The GRIN lenses and the plano-convex lens were mounted in a waterproof stainless steel housing with outer diameter of 1.4 mm and total length of 7.5 mm. Originally designed for a wavelength range of 800–900 nm, this micro-objective lens was used for focusing of 1200 nm 200 femtosecond pulses and collection of back-scattered harmonic and fluorescence photons. An f = 40 mm coupling lens (NA = 0.19, Qioptiq, ARB2 NIR, dia. 25 mm) focused the scanned laser beam in the image plane of the micro-objective lens and forwarded the back-detected harmonic and fluorescence photons to the PMTs (Fig. 9).

We characterized the 2- and 3-photon focusing properties of the GRIN lens, as detailed in the Material and Methods section, using fluorescent microspheres. Lateral (x) and axial (z) resolution values in 2P/3P were: $\Delta_{2P,lateral}$ = 0.7 μm, $\Delta_{2P,axial}$ = 3.5 μm, $\Delta_{3P,lateral}$ = 0.7 μm, and $\Delta_{3P,axial}$ = 3.9 μm, with a measurement error ± 0.1 μm; see Fig. 9(B). We also characterized the lateral and axial resolution of the micro-objective lens in the THG modality by imaging a water-glass interface of a cover-glass slide edge submerged in water (Fig. 9(C)). The normalized axial (z) intensity profile points were fitted with a Gaussian function with FWHM = $\Delta_{THG,axial}$ = 4.4 μm. The normalized lateral (x) intensity profile points were fitted to the error function Erf(x), and lateral THG resolution was measured as the FWHM of the first derivative dErf(x) of the Erf(x). The calculated value of $\Delta_{THG,lateral}$ was 0.9 μm with a measurement error ± 0.1 μm. Theoretically, lateral and axial 2P/3P resolution values can be evaluated for λ = 1200 nm, n = 1.33 (for water as an immersion liquid) and objective NA = 0.8 [59]: $\Delta_{2P,lateral}$ = 0.7 μm, $\Delta_{2P,axial}$ = 3.4 μm, $\Delta_{3P,lateral}$ = 0.6 μm, $\Delta_{3P,axial}$ = 2.8 μm. The experimental and theoretical values of the micro-objective 2P/3P resolution are very close, indicating good performance of the micro-objective lens at the off-design wavelengths.

Figure 10 shows THG/SHG images of brain samples collected with the GRIN micro-objective; the quality of these images is similar to that of the images depicted in Figs. 1 to 6. In Fig. 10(A) and 10(B), we observe neuronal cells in the GM; in Fig. 10(C), the axonal matrix, some fluorescent deposits and low cell density in the WM; and in Fig. 10(D), the high cellularity and vascular proliferation of a high-grade glioma focus, similar to Fig. 5. To collect the images in Fig. 10 we used a power of 50 mW on the sample during 16 seconds. The longer acquisition time results from an almost 7-fold THG signal decrease due to lower bioptic needle objective NA: I_{THG} (NA = 1.1) / I_{THG} (NA = 0.8) = $(1.1 / 0.8)^6 \cong 6.8$.

#258145 Received 25 Jan 2016; revised 8 Mar 2016; accepted 12 Mar 2016; published 18 Apr 2016
(C) 2016 OSA

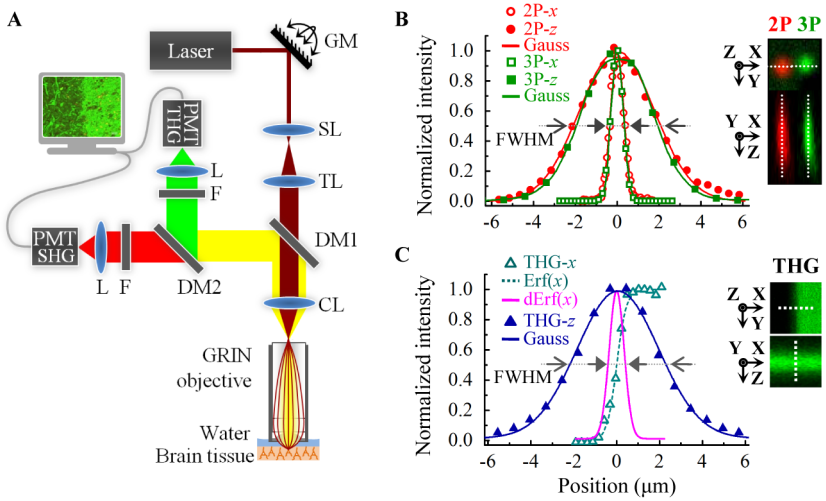

Fig. 9. Endomicroscopic THG/SHG brain tissue imaging. (A) A sketch of the multiphoton microscope equipped with the micro-objective lens. CL – coupling lens. (B and C) Characterization of the lateral and axial resolution of the micro-objective lens. (B) Lateral (x) and axial (z) resolution of the micro-objective lens measured with fluorescent microspheres via two- and three-photon fluorescence (2P, 3P). Line intensity profiles are taken over the lateral (x) and axial (z) images of the 2P/3P fluorescent spheres and are indicated on the inset image with the white dashed lines. Normalized intensity profile points (open and filled circles and squares) are fitted with Gaussian functions (solid lines) and the values of the full-width-at-half-maximum (FWHM) peak widths are measured. (C) Lateral (x) and axial (z) THG resolution of the micro-objective lens measured with a glass-water interface. The inset images show the lateral (x) and axial (z) THG images of the glass-water interface. THG intensity profiles are measured along the white dashed lines indicated on the inset images. The normalized axial (z) intensity profile points (blue filled triangles) are fitted with Gaussian function (solid blue line) and the FWHM was measured to provide the axial THG resolution. The normalized lateral (x) intensity profile points (open teal triangles) are fitted to the error function (dashed teal line), $\mathrm{Erf}(x) = A_1 + 0.5(A_2 - A_1) \times [1 - \mathrm{erf}(A_3 x)]$ with fitting parameters $A_1 = 0.00 \pm 0.01$, $A_2 = 1.00 \pm 0.01$, and $A_3 = 1.90 \pm 0.08$. The lateral THG resolution was measured as the FWHM of the first derivative $\mathrm{dErf}(x)$ of the $\mathrm{Erf}(x)$ (solid magenta line).

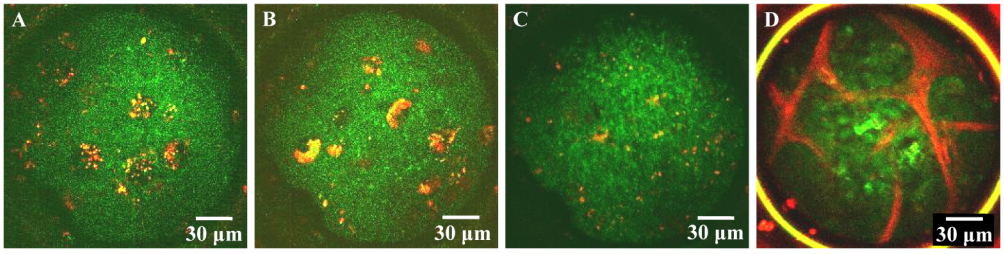

Fig. 10. THG/SHG endomicroscopy of *ex-vivo* human brain tissues. SHG (red) and THG (green) images of healthy and tumor-invaded *ex-vivo* human brain tissue obtained with the micro-objective lens. Each image is a single 4-μm-thick optical section taken at a depth of 20–30 μm below the tissue surface with acquisition time of 16 s and laser power of 50 mW. (A–C) Healthy *ex-vivo* human brain tissue: gray matter neuropil with neuronal somata with lipofuscin content (yellow) (A) and (B); (C) low-cellularity white matter area. (D) High-grade glioma focus.

4. Conclusions

The results shown here provide the first evidence that—by applying the same microscopic criteria that are used by the pathologist, i.e. increased cellularity, nuclear pleomorphism, and rarefaction of neuropil—THG/SHG *ex-vivo* microscopy can be used to recognize the presence

#258145 Received 25 Jan 2016; revised 8 Mar 2016; accepted 12 Mar 2016; published 18 Apr 2016
(C) 2016 OSA

of diffuse infiltrative glioma in fresh, unstained human brain tissue. Images and a first diagnosis can be provided in seconds, with the 'inspection mode', by moving the sample under the scanning microscope (see Visualization 4 and Visualization 5), or in about 5 minutes if an area has to be inspected with sub-cellular detail. The sensitivity of THG to interfaces provides images with excellent contrast in which cell-by-cell variations are visualized. The quality of the images and the speed with which they can be recorded make THG a promising tool for quick assessment of the nature of excised tissue. Importantly, because THG/SHG images are very close to those of histological slides, we expect that the surgeon (or pathologist) will need very little additional training for adequate interpretation of the images. We are planning to construct a THG/SHG *ex-vivo* tabletop device consisting of a compact laser source and a laser-scanning microscope requiring a physical footprint of only 1 m^2, to be placed in an operating room, enabling immediate feedback to the surgeon on the nature of excised tissue, during the operation. With this device, we will perform a quantitative study of the added value of rapid THG/SHG pathological feedback during surgery for the final success of the neurosurgery. Finally, we note that THG/SHG imaging does not induce artifacts associated with fixation, freezing, and staining; therefore, tissue fragments examined *ex-vivo* can still be used for subsequent immunochemical and/or molecular analysis.

The microendoscopy THG/SHG imaging results represent an important step toward the development of a THG/SHG-based bioptic needle, and show that the use of such a needle for *in situ* optical sampling for optimal resection of gliomas is indeed a viable prospect, as has been demonstrated also before for multi-photon microscopies [38,49–54]. Although there are several issues associated with the operation of a needle-like optical device, such as the fact that blood in the surgical cavity may obscure the view, and the fact that only small areas can be biopsied with a needle, it may be a valuable tool in cases where sparing healthy tissue is of such vital importance as in brain surgery. Therefore, the reasonably good quality of the THG images taken with the GRIN micro-objective shown here, together with the developments in the field of microendoscopy, warrant further development of THG/SHG into a true handheld device. This next step, a true handheld bioptic needle, requires an optical fiber to transport the light from a small footprint laser to the GRIN micro-objective, and a small 2D scanner unit, to enable placing the laser at a sufficient distance from the patient. Patient-safe irradiation levels for THG imaging will have to be determined but are expected to lie in the 10–50 mW range [55–58]. This implies that only minor optimization of signal collection efficiency needs to be achieved, because the images of Fig. 10 were measured with 50 mW incident power.

THG/SHG imaging thus holds great promise for improving surgical procedures, thereby reducing the need for second surgeries and the loss of function by excising non-infiltrated brain tissue, as well as improving survival and quality of life of the patients. In addition, the success in the challenging case of diffuse gliomas promises great potential of THG/SHG-based histological analysis for a much wider spectrum of diagnostic applications.

Acknowledgments

We thank H. Lodder for technical support, P. Scholten for her expertise and help with processing the tissue samples after THG imaging. This research is supported by the Dutch Technology Foundation STW (which is part of the Netherlands Organization for Scientific Research (NWO), and which is partly funded by the Ministry of Economic Affairs, Agriculture and Innovation), by a seeding grant of the Neuroscience Campus Amsterdam and by the STOPbraintumors Foundation, The Netherlands, by CNPq – National Council for Scientific and Technological Development, Brazil.

#258145 Received 25 Jan 2016; revised 8 Mar 2016; accepted 12 Mar 2016; published 18 Apr 2016
(C) 2016 OSA